J Solid State Electrochem (2008) 12:1541–1548
DOI 10.1007/s10008-008-0508-4

ORIGINAL PAPER

Underpotential surface reduction of mesoporous CeO_2 nanoparticle films

Charles Y. Cummings · Susan J. Stott · Michael J. Bonné · Karen J. Edler · Pauline M. King · Roger J. Mortimer · Frank Marken

Received: 6 December 2007 / Revised: 27 December 2007 / Accepted: 30 December 2007 / Published online: 25 January 2008

Abstract The formation of variable-thickness CeO_2 nanoparticle mesoporous films from a colloidal nanoparticle solution (approximately 1–3-nm-diameter CeO_2) is demonstrated using a layer-by-layer deposition process with small organic binder molecules such as cyclohexanehexacarboxylate and phytate. Film growth is characterised by scanning and transmission electron microscopies, X-ray scattering and quartz crystal microbalance techniques. The surface electrochemistry of CeO_2 films before and after calcination at 500 °C in air is investigated. A well-defined Ce(IV/III) redox process confined to the oxide surface is observed. Beyond a threshold potential, a new phosphate phase, presumably $CePO_4$, is formed during electrochemical reduction of CeO_2 in aqueous phosphate buffer solution. The voltammetric signal is sensitive to (1) thermal pretreatment, (2) film thickness, (3) phosphate concentration and (4) pH. The reversible 'underpotential reduction' of CeO_2 is demonstrated at potentials positive of the threshold. A transition occurs from the reversible 'underpotential region' in which no phosphate phase is formed to the irreversible 'overpotential region' in which the formation of the cerium(III) phosphate phase is observed. The experimental results are rationalised based on surface reactivity and nucleation effects.

C. Y. Cummings · M. J. Bonné · K. J. Edler · F. Marken (✉)
Department of Chemistry, University of Bath,
Bath BA2 7AY, UK
e-mail: f.marken@bath.ac.uk

S. J. Stott · P. M. King · R. J. Mortimer
Department of Chemistry, Loughborough University,
Loughborough LE11 3TU, UK

Keywords CeO_2 · Nanoparticle · Assembly · ITO · Cyclic voltammetry · Electroanalysis · Electrocatalysis · Underpotential reduction · Sensor

Introduction

Ceria, CeO_2, is used widely as a technical material in a number of applications including polishing [1] and membrane filtration [2]. Nanoparticulate ceria has been used as a substrate for heterogeneous catalysts, as a promoter for water gas shift and steam reforming reactions [3] and as a high oxygen storage/buffer material [4], and it is a component in automobile exhaust systems [5]. Further applications of CeO_2 include thin films for anti-corrosion coatings [6] and in solid oxide fuel cells [7]. In electrochromism, CeO_2 thin films have been employed in smart windows as ion storage materials or counter electrodes [8] because of a high optical transparency in the visible region and the ability to exchange cations and electrons [9]. CeO_2 may be regarded (and often is) as an inert oxide with little electrochemical activity [10, 11]. However, it is shown here that CeO_2 is electrochemically highly active, and it exhibits a rich surface electrochemistry, for example in aqueous buffer media.

To study the surface electrochemistry of CeO_2, mesoporous films of high surface area need to be deposited onto the electrode surface. CeO_2 can be obtained commercially in the form of an aqueous sol of 1–3-nm-diameter nanoparticles. These particles exhibit a positive surface charge (p.z.c. 8.1 [12]), and they are readily adsorbed onto suitable electrode surfaces such as tin-doped indium oxide (ITO). Furthermore, by applying suitable binder molecules [13], multi-layer films can be formed, and the thickness of the resulting mesoporous CeO_2 surface layer can be controlled.

The surface electrochemical reactions of mesoporous CeO_2 are shown to strongly depend on the solution environment. Potential applications of the surface redox processes could be envisaged in electroanalysis (based on the redox-induced compositional changes) or, perhaps more likely, in electrocatalysis (exploiting the surface redox system to replace well-known homogeneous Ce^{4+}-driven redox processes, possibly in organic solvent media).

It is shown here that the electrochemical response of CeO_2 in aqueous media is similar to those reported for TiO_2 with the important difference that CeO_2 is much more reactive towards phosphate anions. A new interfacial phosphate phase is formed during reduction of Ce(IV) but only when a negative threshold potential is reached. For the reversible electrode process associated with the potential range positive of the threshold potential, the term 'underpotential reduction' is proposed. A chemical interpretation for the change in reactivity at the threshold potential is suggested.

Experimental

Chemicals

Deionised and filtered water was taken from an Elga water purification system (Elga, High Wycombe, Bucks, UK) with a resistivity of not less than 18 MΩ cm. Ceria sol (diameter determined as approximately 1–3 nm, 20 wt% in aqueous HNO_3, pH 2–3) was obtained from Nyacol Nano Technologies, MA, and diluted 10- or 50-fold with deionised water. Phytic acid dodecasodium salt hydrate, 1,2,3,4,5,6-cyclohexanehexacarboxylic acid monohydrate, NaOH, H_3PO_4, KCl, KOH, K_2CO_3, K_2HPO_4 and KH_2PO_4 were obtained commercially in analytical or the highest purity grade available and used without further purification.

Instrumentation

Voltammetric measurements were performed with a computer controlled Eco Chemie PGSTAT20 Autolab potentiostat system. Experiments were conducted in staircase voltammetry mode with a platinum gauze counter electrode and saturated calomel reference electrode (SCE, REF401, Radiometer). The working electrode was a ITO-coated glass (10×60 mm, resistivity 20 Ω per square) with approximately 8% tin, obtained from Image Optics Components (Basildon, Essex). The ITO electrode surface was cleaned by 30-min heating at 500 °C in air, re-equilibrated to ambient conditions for at least 1 h and then modified with the porous cerium oxide film. Before conducting electrochemical experiments, all solutions were purged with argon (BOC, UK). All experiments were carried out at a temperature of 22±2 °C. An Elite tube furnace system was employed for cleaning ITO electrode surfaces (at 500 °C in air) and for calcining metal oxide binder films (at 500 °C in air).

A quartz crystal oscillator circuit (Oxford Electrodes) connected to a frequency counter (Fluke, PM6680B) allowed the resonance frequency of the ITO quartz crystal sensor to be monitored simultaneously to conducting voltammetric experiments. A Faraday cage was used to contain the quartz crystal to minimise noise interference. The analogue output of the counter was fed into the ADC input of an Autolab potentiostat system (Eco Chemie, The Netherlands), and data processing was possible with GPES software (Eco Chemie). For data analysis, the Sauerbrey equation was employed: $\frac{\Delta m}{\Delta f} = -\frac{A\sqrt{\mu_Q \rho_Q}}{2f_0^2}$, with the area, A= 0.2 cm^2. The measured frequency change corresponds to a mass increase with $\frac{\Delta m}{\Delta f} = -1.05$ ng Hz^{-1}. Layer-by-layer deposition processes were monitored with the crystal suspended in air. Droplets of solution were applied to one side of the ITO-coated crystal, and after rinsing and drying, the frequency was measured and monitored layer-by-layer.

Scanning electron microscopy images were obtained with a Leo 1530 Field Emission Gun Scanning Electron Microscope (FEGSEM) system. Before FEGSEM imaging, the sample surface was scratched with a scalpel blade. Transmission electron microscopy (TEM) images were obtained on a JEOL JEM1200 TEM. X-ray diffraction (XRD) measurements were obtained on a Bruker D8 Advance powder diffractometer fitted with a position-sensing detector and using Cu $K_{\alpha 1}$ radiation. A simultaneous small-angle X-ray scattering and wide-angle X-ray scattering pattern (SAXS/WAXS) of the CeO_2 films was obtained on a SAXSess system using a PW3830 X-ray generator, and the X-ray image plates were observed using a Perkin-Elmer cyclone storage phosphor system. CeO_2 films on a microscopy cover plate were produced and the patterns recorded in transmission mode with Cu K_α radiation (1λ =1.5406 Å) at 40 kV and 50 mA with an exposure time of 20 min. A background pattern from a clean cover plate was subtracted, and the data were corrected for slit smearing before fitting.

Deposition and electrode preparation procedures

Deposition of multi-layer mesoporous films of metal oxide and organic binder on ITO glass electrodes followed a layer-by-layer dip-coating method [14] initially developed for polyelectrolyte systems by Decher [15]. A clean ITO surface (washed with ethanol and deionised water, dried and treated 30 min at 500 °C in air) was dipped into a solution of CeO_2 nanoparticles (2 wt%) followed by rinsing with deionised water. By dipping the resulting nanoparticle deposit into a solution of binder molecule such as cyclohexanehexacarboxylic acid (10 mM in water) or phytic acid (40 mM in pH 3 aqueous solution) and rinsing, it is

possible to reverse the surface charge. The dipping process was undertaken using a robotic Nima dip-coating carousel (DSG—Carousel, Nima Technology, Coventry, UK) and repeated to give multi-layer deposits.

Results and discussion

Layer-by-layer deposition of CeO_2 with molecular binders

In this investigation, the deposition of CeO_2 nanoparticles onto a clean ITO electrode surface occurs spontaneously upon dipping the electrode into a ceria sol. Figure 1 shows a typical SEM image of the film deposit with a scratch line indicating a clean electrode surface. Additional TEM imaging of the nanoparticles reveals that the particle diameter is typically 1–3 nm (see Fig. 1c). This suggests that the first "monolayer" shown in Fig. 1a is actually dominated by aggregates of nanoparticles. It is possible to immerse the 'monolayer' of CeO_2 particles into a solution of appropriate binder and to build up multiple CeO_2 layers on the ITO-coated glass surface (see "Experimental"). Figure 1b shows a typical 20-layer deposit after calcination (thermal removal of all organic components at 500 °C), and the porous structure is clearly evident.

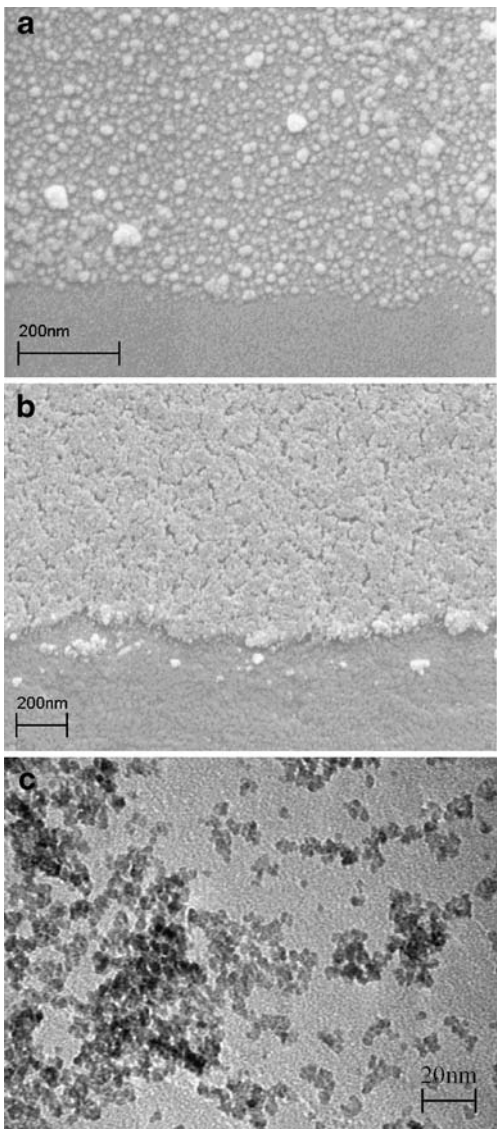

Fig. 1 FEGSEM images of CeO_2 nanoparticles (approximately 1–3 nm diameter) deposited layer-by-layer with phytic acid binder onto the surface of an ITO-doped glass slide. In **a**, a single-layer CeO_2 deposit with some aggregates and in **b** a 20-layer deposit after furnace treatment are shown. **c** TEM image of individual nanoparticles and aggregates

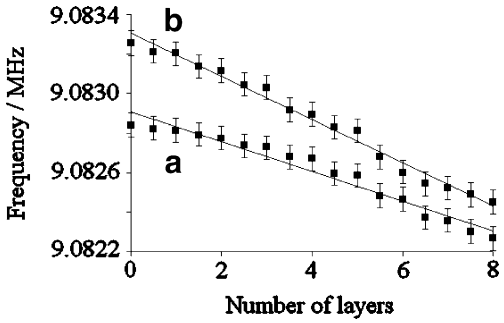

Fig. 2 Plot of the resonance frequency change for an ITO-coated quartz crystal during layer-by-layer deposition of **a** CeO_2 with phytic acid and **b** CeO_2 with CHHCA

The electron microscopy data in Fig. 1 are supported by experiments with a quartz crystal oscillator balance conducted in air. Figure 2 shows the subsequent reduction in the resonance frequency of an ITO-coated quartz crystal resonator during the layer-by-layer deposition process of CeO_2 with the two binder molecules, phytate (see Fig. 2a) and cyclohexanehexacarboxylate (CHHCA, see Fig. 2b).

For the deposition of CeO_2 with phytic acid, each layer is consistent with approximately 72 Hz change corresponding to 76 ng (assuming a rigid film according to the Sauerbrey equation [16]). Detailed analysis gives a weight of approximately 60 ng CeO_2 and 16 ng phytic acid (molecular weight 924 g mol^{-1}). For the deposition of CeO_2 with CHHCA, each layer is consistent with a 100-Hz change corresponding to 105 ng, which splits into a weight of approximately 70 ng CeO_2 and 35 ng CHHCA (molecular weight 366 g mol^{-1}). Humidity effects are not considered in this analysis but could be substantial.

The porosity of the mesoporous CeO_2 films before and after calcination was further investigated with SAXS/WAXS techniques. Based on XRD data (not shown), the cubic CeO_2 (ceranite) crystal structure is maintained during the calcination process. However, the average particle size is changing. Figure 3b shows that freshly deposited CeO_2–CHHCA films are composed of nanoparticles with approximately 2 nm average diameter (the same average diameter is observed for solution phase nanoparticles, see Fig. 3a). After calcination at 500 °C, the average diameter is

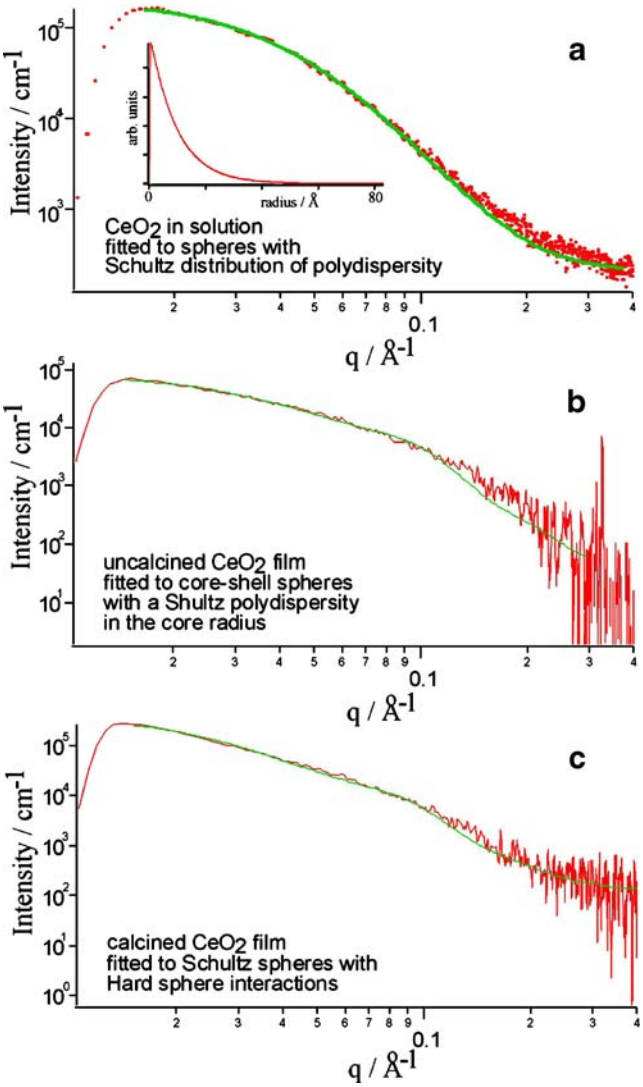

Fig. 3 SAXS/WAXS data for **a** the CeO_2 nanoparticle solution (20 wt %, aqueous; *red*, experimental data; *green*, simulation with mean radius 0.945 nm and polydispersity 0.99; *inset*, Schultz distribution), **b** a CeO_2–CHHCA film deposit (*red*, experimental data; *green*, simulation with average core radius 1.093 nm, core polydispersity 1.0 and shell thickness 0.46 nm) and **c** a CeO_2–CHHCA film deposit after calcination (*red*, experimental data; *green*, simulation with mean radius 1.847 nm and polydispersity 0.9)

increased to approximately 3.9 nm, although the volume fraction remains at approximately 20%. The polydispersity (Schultz) is high for all samples (see Fig. 3).

Electrochemical reactivity of CeO_2 nanoparticle mono- and multi-layers

The monolayer of CeO_2 nanoparticles formed on ITO electrode surfaces is electrochemically active. Voltammograms shown in Fig. 4 have been obtained in aqueous 0.1 M KCl (see Fig. 4i–iii) and in 0.1 M phosphate buffer solution (see Fig. 4iv and v). In the presence of KCl, a strong reduction response starting at a potential of 0.25 V vs SCE is clearly detected. This reduction response is reversible, and upon scanning the potential positive, a corresponding oxidation response is observed. The voltammetric signal remains stable over several potential cycles and is tentatively attributed to a $Ce^{4+/3+}$ process at the nanoparticle surface similar to processes observed with TiO_2 [17] or SnO_2 [18] nanoparticle films.

It is interesting to compare the charge under the reduction response with the estimated amount of CeO_2 on the electrode surface. Integration of the charge under the voltammetric response shown in Fig. 4iii gives approximately 80 μC. In comparison, for a monolayer of 1–3-nm-diameter CeO_2 particles, an expected charge for a one-electron process of 0.4 mC can be calculated. Therefore, roughly about 20% of the deposit is electrochemically reduced and re-oxidised with a scan rate of 0.1 V s^{-1} and immersed in aqueous 0.1 M KCl. It can be assumed that predominantly the surface (and possibly also a hydrous CeO_2 surface layer) of the CeO_2 nanoparticles is affected. The degree of reduction/conversion appears to

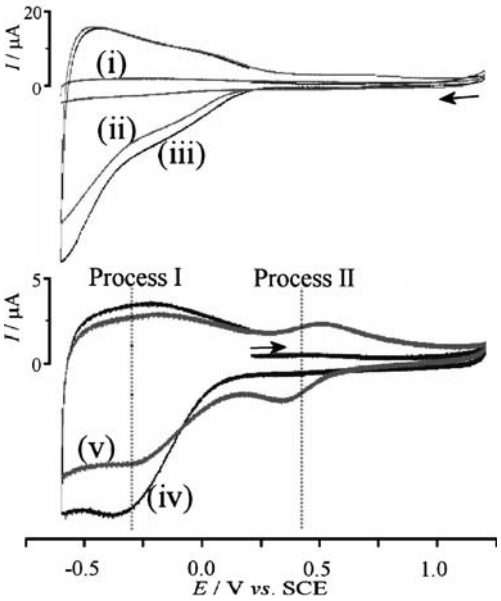

Fig. 4 *i*, Cyclic voltammogram (scan rate 100 mV s^{-1}) of a clean ITO glass electrode with no CeO_2 deposit in aqueous 0.1 M phosphate buffer solution at pH 7. *ii–iii*, Cyclic voltammogram (two consecutive scans, scan rate 100 mV s^{-1}) obtained for the reduction of CeO_2 in aqueous 0.1 M KCl at a single-layer CeO_2 deposited on an ITO glass electrode. *iv–v*, Cyclic voltammogram (two consecutive scans, scan rate 100 mV s^{-1}) obtained for one-layer CeO_2 nanoparticles absorbed onto ITO and immersed in aqueous 0.1 M phosphate buffer solution at pH 7 showing an electrochemical response at a potential of E_{mid}=−0.28 V vs SCE characteristic for the Ce(IV/III) redox system (process I). In the presence of phosphate, the reduction of CeO_2 is followed by a new voltammetric signal at E_{mid}=0.42 V vs SCE. This process can be identified as an interfacial Ce(IV/III) phosphate redox system (process II)

depend strongly on the applied potential but not significantly on the applied scan rate.

Cyclic voltammograms obtained in the presence of phosphate anions reveal distinct differences (see Fig. 4iv–v). The initial reduction process at E_{mid}=−0.28 V vs SCE is now considerably smaller in current (see process I), and after the first potential cycle, a new voltammetric response is detected at a potential of E_{mid}=0.42 V vs SCE (see process II). The signal associated with process II only occurs after reduction in process I and a gradual change with currents for process I decreasing and currents for process II increasing is observed upon continuous potential cycling (see Fig. 4). Therefore, a slow chemical conversion step, presumably the formation of a solid cerium phosphate phase, must be responsible for this transformation. To prove this hypothesis, cerium(III) phosphate was prepared by direct precipitation from the Ce^{3+} solution with phosphate. A clean ITO electrode brought into contact with the $CePO_4$ precipitate dried in air and re-immersed in aqueous 0.1 M phosphate buffer shows voltammetric responses (not shown) only for process II. Therefore, process II is identified as the $Ce^{4+/3+}$ phosphate redox system present most likely on the surface of the CeO_2 nanoparticles.

In comparison to the similar experiments for TiO_2 films [19], the more inert nature of the TiO_2 with respect to CeO_2 allows charging and discharging processes to occur reversibly. The difference in behaviour can be explained based on differences in the crystal structure of TiO_2 (anatase) and CeO_2 (ceranite). The former anatase structure has Ti^{4+} coordinated in a distorted octahedron with bond distances of 1.96 to 2.05 Å. In contrast, in ceranite, Ce^{4+} is coordinated to eight oxygen atoms in a cubic arrangement with 2.34 Å bond length. The Ce^{4+}–O^{2-} bond is therefore more labile, and after reduction to Ce^{3+}, more facile ligand exchange may occur.

To obtain more information about this complex redox system, experiments were conducted in different concentrations of phosphate and at various proton activities. Figure 5 shows the effect of phosphate concentration. The reduction response for process I can clearly be seen to depend on the phosphate concentration. The higher the phosphate concentration, the faster is this voltammetric signal diminished. Continuous potential cycling leads to a simultaneous increase in peak currents for process II.

Figure 5d shows a comparison of the 15th scan of cyclic voltammograms for phosphate concentrations of 100, 10, 1

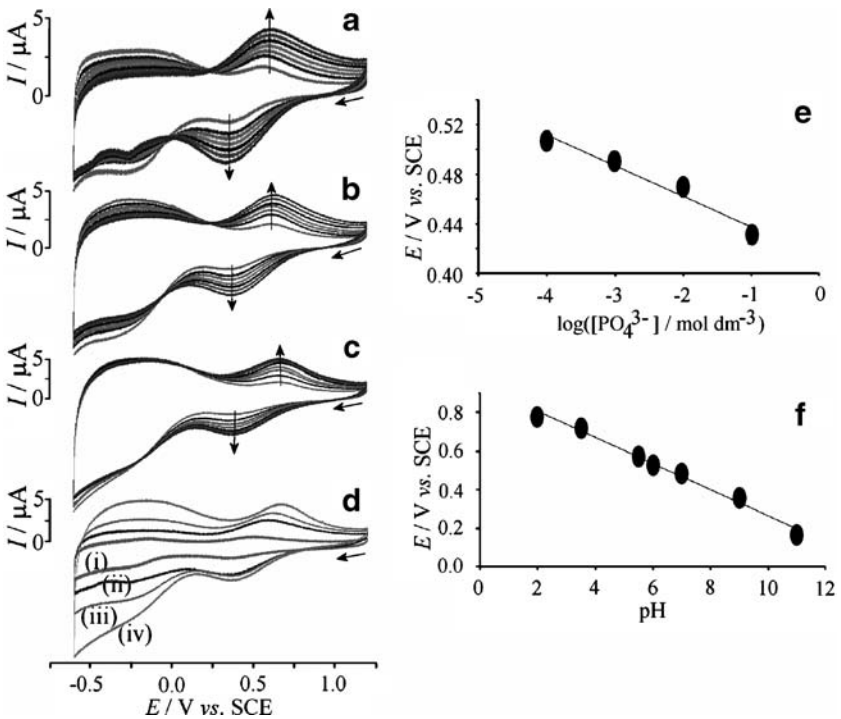

Fig. 5 Multi-cycle voltammograms (scan rate 100 mV s^{-1}) for ITO electrodes with one-layer CeO_2 in the presence of **a** 10, **b** 1 and **c** 0.1 mM phosphate buffer solution pH 7 and 0.1 M KCl. **d** Overlay showing a comparison of the final scan for (*i*) 100, (*ii*) 10, (*iii*) 1 and (*iv*) 0.1 mM phosphate buffer in 0.1 M KCl. **e** Plot of the midpoint potential for process II vs SCE for a single layer of CeO_2 on ITO vs the log phosphate concentration (pH 7). **f** Plot of the midpoint potential for process II vs SCE for a single layer of CeO_2 on ITO vs the pH

and 0.1 mM. A clear trend is observed with higher phosphate concentrations reducing the voltammetric responses. Apparently, phosphate is accelerating the formation of cerium phosphate probably because of a more facile surface reaction in the presence of higher phosphate concentrations.

The midpoint potential for process II is sensitive to both phosphate concentration and proton activity (see Fig. 5e and f), and the slopes observed are 24 mV per decadic change in phosphate concentration and 62 mV per pH unit. This allows process I and process II to be tentatively assigned (see Eqs. 1 and 2).

$$\text{Process I}: 2CeO_{2(\text{surface})} + 2e^- + 2H^+ \rightarrow Ce_2O_{3(\text{surface})} + H_2O \quad (1)$$

$$\text{Process II}: Ce_3(PO_4)_{4(\text{surface})} + 3e^- + 3H^+ \rightarrow 3CePO_{4(\text{surface})} + H_3PO_4 \quad (2)$$

The product of the reduction reaction in process I, Ce_2O_3, is assumed to react with phosphate in the aqueous solution phase to give $CePO_4$ at the surface of the nanoparticle deposit. It is likely that solid structures are formed in a highly hydrated state. This can be further supported with the increase in the voltammetric response as a function of film thickness and the effect of calcination (see below).

Figure 6 shows multi-cycle voltammograms obtained for ITO electrodes with multi-layer CeO_2 phytate film deposits after calcining (at 500 °C in air, see "Experimental") in the presence of 1 mM phosphate buffer at pH 7. As seen in the experiments without calcination, a gradual change in the peak current is observed upon scanning to negative potentials for process I and for process II. Process II is observed (very weak current response, not observed in Fig. 6c and d) in the first cycle probably because of the presence of phosphate from phytate during calcinations. XRD powder diffraction experiments show that the cubic fluorite crystal structure of CeO_2 is not changed during the calcining process at 500 °C (not shown).

By doubling the amount of CeO_2 phytate film deposited onto the ITO electrode surface, the peak current recorded is approximately doubled (see Fig. 6). Calcining the metal oxide films is also shown to overall increase the current response close to the value observed for the CeO_2 monolayer in aqueous KCl (see Fig. 4, approximately 80 μC per layer, consistent with about 20% conversion). The presence of the phosphate phase appears to be reducing the current responses (because of the electronic blocking effect of the interfacial phosphate layer, see Fig. 5), but well-defined responses are observed with only 1 mM phosphate buffer present. When compared to the behaviour of non-calcined films (see Fig. 5b), the formation of the cerium phosphate product on calcined films appears to be significantly slower possibly because of the lack of reactive hydrous CeO_2 and a lower reactivity of the CeO_2 surface sites. In addition, an increase in electrical conductivity through the oxide may be possible as an electron transport through the slightly sintered oxide structure may be enhanced because of lower inter-particle distances.

Next, a similar set of experiments was conducted using 1,2,3,4,5,6-cyclohexanehexacarboxylic acid monohydrate

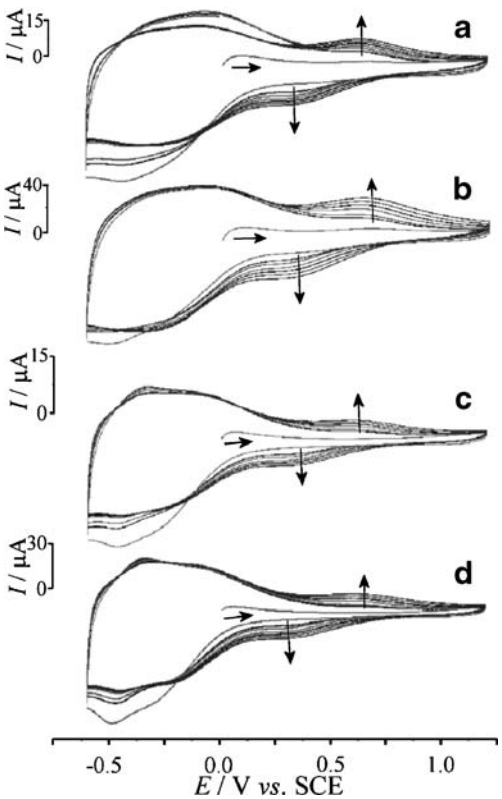

Fig. 6 **a** Cyclic voltammograms (scan rate 100 mV s^{-1}) for the reduction of a two-layer CeO_2 phytate film on ITO after calcination. The electrode is immersed in 1 mM phosphate buffer at pH 7 in aqueous 0.1 M KCl. **b** Cyclic voltammograms (scan rate 100 mV s^{-1}) for the reduction of a four-layer CeO_2 phytate film on ITO after calcination. The electrode is immersed in 1 mM phosphate buffer at pH 7 in aqueous 0.1 M KCl. The first scan and the ten following scans are shown. Also shown are multi-layer cyclic voltammograms (scan rate 100 mV s^{-1}) for **c** a two-layer and **d** a four-layer deposit of CeO_2–CHHCA on ITO, after heat treatment at 500 °C, and immersed in aqueous 1 mM phosphate buffer solution pH 7 and 0.1 M KCl

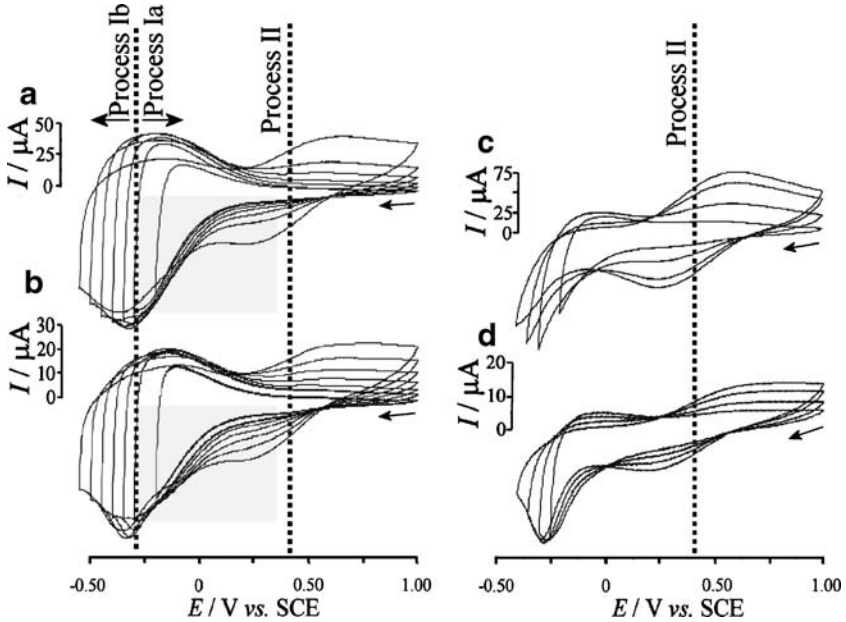

Fig. 7 Cyclic voltammograms (scan rate 100 mV s^{-1}) for the reduction of **a** a eight-layer and **b** a four-layer CeO_2 phytate film on ITO after calcination and immersed in 0.1 M phosphate buffer at pH 7. Cyclic voltammograms (scan rate 100 mV s^{-1}) for the reduction of **c** a eight-layer and **d** a four-layer CeO_2 phytate film on ITO as deposited (not calcined) and immersed in 0.1 M phosphate buffer at pH 7. In all cases, the effect of the negative switching potential is shown. The *grey zone* from +0.4 to −0.25 V vs SCE corresponds to the "underpotential reduction" region

(CHHCA) as a binder in the place of the phytic acid. In Fig. 6c and d, the multi-cycle voltammograms obtained for ITO electrodes with multi-layer CeO_2 CHHCA deposits in the presence of 1 mM phosphate are shown. As with the phytic acid binder, the expected changes in peak current corresponding to processes I and II are clearly being generated. This indicates that not only does CHHCA function as a good binder for metal oxide particles such as CeO_2 but also enables the study of process II without the possible interference of the phosphate from the phytic acid binder molecules.

Underpotential ($Ce^{4+/3+}$) surface reduction processes in aqueous phosphate media

To investigate the electrochemical phase transformation from CeO_2 to $CePO_4$ in more detail, voltammograms were obtained as a function of the negative switching potential. Figure 7 shows typical sets of voltammograms obtained for calcined and non-calcined CeO_2 phytate films with four- or eight-layer thickness.

Calcined CeO_2 films can be seen to convert much less rapidly when compared to the non-calcined samples that convert to $CePO_4$ even during the early stages of the reduction process. It is likely that the non-calcined nanoparticles are surrounded by a shell of highly hydrated CeO_2, which after reduction is highly reactive towards phosphate. In the case of the calcined CeO_2 films, the reduction proceeds to a threshold potential of approximately −0.25 V vs SCE without producing $CePO_4$, and only beyond this point, the conversion becomes facile. It is possible to distinguish an

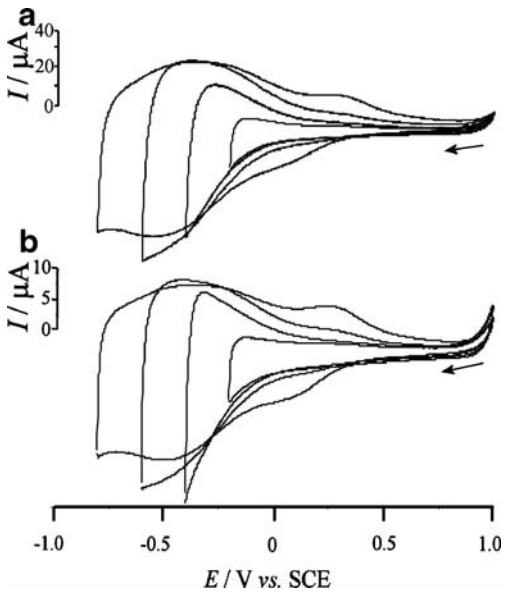

Fig. 8 Cyclic voltammograms (scan rate 100 mV s^{-1}) for the reduction of **a** an eight-layer and **b** a four-layer CeO_2–CHHCA film on ITO (after calcination) immersed in 0.01 M phosphate buffer at pH 7

underpotential reduction region (process Ia) and an overpotential reduction region (process Ib; see Eqs. 3 and 4).

$$\text{Process Ia}: 2CeO_{2(\text{surface})} + 2e^- + 2H^+ \rightarrow Ce_2O_{3(\text{surface})} + H_2O \quad (3)$$

$$\text{Process Ib}: CeO_{2(\text{surface})} + e^- + 4H^+ + PO_4^{3-} \rightarrow CePO_{4(\text{surface})} + 2H_2O \quad (4)$$

Surface sites affected in the underpotential reduction region appear to be less susceptible to the formation of $CePO_4$ possibly because of being more strongly bound into the oxide matrix. By increasing the coverage of the oxide surface with reduced Ce(III) states, the oxide support weakens, and at a sufficiently negative threshold potential, the formation of $CePO_4$ commences (possibly associated with a nucleation step).

Figure 8 shows cyclic voltammograms obtained for the reduction of CeO_2–CHHCA immersed in 0.01 M phosphate buffer at pH 7. Again, the transition from chemically reversible (process Ia) to irreversible (process Ib) is observed this time at approximately −0.4 V vs SCE. The 'underpotential reduction' effect is very similar to the 'underpotential deposition' effect in that a surface layer is formed before bulk transformation. The current responses scale with the number of deposited CeO_2–CHHCA layers.

Conclusions

It has been shown that CeO_2 in the form of thin mesoporous films is electrochemically active. A reduction assigned to a $Ce^{4+/3+}$ process has been observed, and follow-up chemical processes in the presence of phosphate have been discovered. The interfacial formation of $CePO_4$ has been proven, and effects of the type and thickness of deposit, the phosphate concentration and pH on the process have been analysed. A threshold potential and an underpotential reduction region have been observed.

In the future, it will be possible to exploit the ability of CeO_2 nanoparticles to form surface species with ligands other than phosphate and to give distinct electrochemical properties to the CeO_2 nanoparticle surface, e.g. for electrocatalytic processes. The importance of Ce^{4+} as an oxidation reagent in organic chemistry could lead to novel surface electrochemical processes with a heterogeneous recyclable Ce(IV) system.

Acknowledgements S.J.S. is grateful for the analytical science studentship awarded by the RSC and the EPSRC. Hugh Perrott (Department of Physics, University of Bath) is gratefully acknowledged for assistance with electron microscopy imaging.

References

1. Yuan JL, Lu BH, Lin X, Zhang LB, Ji SM (2002) J Mater Process Technol 129:171
2. Siriwardane RV, Poston Jr JA, Fisher EP, Lee TH, Dorris SE, Balachandran U (2003) Appl Surf Sci 217:43
3. Astruc D (ed) (2008) In: Nanoparticles and catalysis. Wiley-VCH, Weinheim (p 517)
4. Uy D, O'Neill AE, Xu L, Weber WH, McCabe RW (2003) Appl Catal B 41:269
5. Matsumoto S (2004) Catal Today 90:183
6. Mora N, Cano E, Polo JL, Puente JM, Bastidas JM (2004) Corros Sci 46:563
7. Ma J, Zhang TS, Kong LB, Hing P, Chan SH (2004) J Power Sources 132:71
8. Granqvist CG, Azens A, Hjelm A, Kullman L, Niklasson GA, Ronnow D, Stromme Mattsson M, Veszelei M, Vaivars G (1998) Sol Energy 63:199
9. Veszelei M, Stromme Mattsson M, Kullman L, Azens A, Granqvist CG (1999) Sol Energy Mater Sol Cells 56:223
10. For a review see Mogensen M, Sammes NM, Tompsett GA (2000) Solid State Ionics 129:63
11. Bard AJ (ed) (1976) In: Encyclopedia of electrochemistry of the elements. vol. VI. Marcel Dekker, New York (Chapter VI-2)
12. Defaria LA, Trasatti S (1994) J Coll Interface Sci 167:352
13. McKenzie KJ, Marken F (2003) Langmuir 19:4327
14. McKenzie KJ, Marken F, Hyde M, Compton RG (2002) New J Chem 26:625
15. Decher G, Schlenoff JB (2003) Multilayer thin films. Wiley, Weinheim
16. Ward MD (1995) In: Rubinstein I (ed) Physical electrochemistry. Marcel Dekker, New York, p 293
17. Milsom EV, Perrott HR, Peter LM, Marken F (2005) Langmuir 21:9482
18. Milsom EV, Dash HA, Jenkins TA, Halliwell CM, Thetford A, Bligh N, Nogala W, Opallo M, Marken F (2007) J Electroanal Chem 610:28
19. Marken F, Bhambra AS, Kim DH, Mortimer RJ, Stott SJ (2004) Electrochem Commun 6:1153